ACS APPLIED MATERIALS & INTERFACES

Research Article

www.acsami.org

Enhanced Photocatalytic Hydrogen Production Activities of Au-Loaded ZnS Flowers

Jiye Zhang,[†] Yonghao Wang,[†] Jun Zhang,[‡] Zhang Lin,[§] Feng Huang,*[,†] and Jiaguo Yu*[,‡]

[†]Key Laboratory of Optoelectronic Materials Chemistry and Physics and [§]State Key Lab of Structural Chemistry, Fujian Institute of Research on the Structure of Matter, Chinese Academy of Sciences, Fuzhou, Fujian, 350002, China

[‡]State Key Laboratory of Advanced Technology for Material Synthesis and Processing, Wuhan University of Technology, Luoshi Road 122#, Wuhan, Hubei, 430070, China

ABSTRACT: Au-nanoparticle-decorated ZnS nanoarchitectures were fabricated by a simple hydrothermal approach combined with a deposition-precipitation method. After the deposition-precipitation process, 5-nm Au nanoparticles were homogeneously dispersed on the ZnS surface. In addition, the band gap of ZnS was also narrowed by the incorporation of a small amount of Au(I) ions. The photocatalytic hydrogen production activities of all the samples were evaluated by using Na_2S and Na_2SO_3 as sacrificial reagents in water under a 350 W xenon arc lamp. The results show that the photocatalytic hydrogen production rate of ZnS nanoarchitectures can be significantly improved by loading Au cocatalysts and reaches an optimal value (3306 μmol h^{-1} g^{-1}) at the Au content of 4% wt. Although strong surface plasmon resonance (SPR) absorption of the Au nanoparticles was found in the Au-loaded samples, all of these samples exhibit no activities in the visible light region (λ > 420 nm). On the basis of this Au/ZnS system, the possible roles of Au deposition in improving the photocatalytic hydrogen production activity, especially the necessary condition for SPR effect of metal nanostructures to function in the visible-light photocatalysis, are critically discussed.

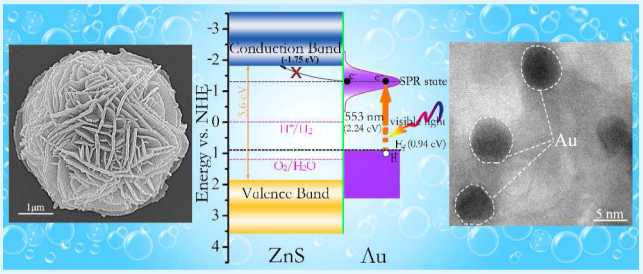

KEYWORDS: *ZnS nanoarchitecture, gold, surface plasmon resonance, photocatalysis, hydrogen production, charge transfer*

INTRODUCTION

Hydrogen, a clean and renewable energy source, has become even more attractive with the depletion of fossil fuel reserves and the deterioration of the global environment.[1,2] The prevalent method of hydrogen production is steam reforming of natural gas,[2] which still consumes nonrenewable resources. Several sustainable sources of H_2 from biomass were proposed as alternatives.[3] However, the economic efficiency of using biomass sources remains to be seen.[4] In view of the abundance of water on the earth, the most desirable hydrogen production should be from the direct splitting of water. Since the pioneering work of Fujishima and Honda in 1972,[5] interest in the field of semiconductor photocatalytic water splitting was catalyzed by the prospect that it would become a low-cost and eco-friendly way to produce hydrogen directly from sunlight and water. Consequently, various semiconductors, including the celebrated TiO_2, were proposed to serve as photocatalysts for photoelectrochemical water splitting.[6−12] Among them, ZnS is widely investigated owing to its relatively high activity for H_2 evolution even without any assistance of noble metal cocatalysts.[13,14] As a direct band gap semiconductor, the theoretical efficiency of photocarrier generation of ZnS is much higher than that of TiO_2, which may be greatly beneficial to the photocatalytic activity. Actually, some ZnS materials show better photocatalytic activities than TiO_2.[15] Nevertheless, the photocatalytic efficiency of ZnS is seriously restricted by the fast recombination of photoexcited charge carriers. Moreover, like TiO_2, ZnS possesses a wide bandgap (~ 3.6 eV),[16] which may limit its ability for solar energy harvesting. Therefore, the photocatalytic activity of ZnS can still be greatly improved. ZnS may become a promising photocatalyst for effective solar water splitting, when its visible light response is enhanced and the direct recombination of charge carriers is suppressed.

Therefore, enormous efforts have been dedicated to either narrowing the band gap of ZnS or reducing the recombination of photogenerated charge carriers. For instance, ZnS was alloyed with various narrow bandgap semiconductors to extend its photoresponse to the visible-light region.[17−19] On the other hand, to accelerate the separation of photogenerated charge carriers, ZnS was combined with other semiconductors (TiO_2, CuS, etc.)[13,20,21] or metals to fabricate various heterostructures.[22−24] According to the present research results, noble metal/ZnS composites may become a possible solution to remarkably improve the photocatalytic hydrogen production activity of ZnS. More specifically, the electric field induced in the interface of metal/ZnS heterostructures can effectively separate the photogenerated charge carriers. Decorating the ZnS surface with small noble metal particles can create

Received: November 16, 2012
Accepted: December 27, 2012
Published: December 27, 2012

separation centers for electron−hole pairs as well as active sites for hydrogen evolution.[25,26] Furthermore, noble metal nanostructures deposited on ZnS surface may extend the spectral response to visible light region because of the surface plasmon resonance (SPR) effect.[27,28]

In this work, we present a Au/ZnS hybrid system fabricated by a simple hydrothermal and deposition-precipitation method. The self-supported ZnS nanoarchitecture with exposed wurtzite (0001) facets were chosen as the candidate for Au nanoparticle loading, which itself exhibit superior photocatalytic activity owing to the internal electric field induced by the spontaneous polarization of the wurtzite [0001] direction. After Au nanoparticle loading, the photocatalytic activity of the ZnS nanoarchitectures was found substantially improved. The physiochemical properties of a series of Au-nanoparticle-decorated ZnS nanoarchitectures as well as the effect of the Au loading content on their photocatalytic H_2-production rate from aqueous solutions containing Na_2S and Na_2SO_3 were extensively characterized and investigated. With regard to ZnS system, the roles of Au cocatalysts in the photocatalytic hydrogen production process are discussed, including the charge separation effect, band gap narrowing, and the SPR effect. Then, the necessary conditions for SPR effect of metal nanostructures to function in the visible-light photocatalysis are proposed.

EXPERIMENTAL SECTION

Chemicals. All the chemicals in this work, including NaOH, Na_2S, ZnO, and $HAuCl_4$, were AR reagents purchased from Sinopharm Chemical Reagent Co. Ltd. and were used without any further purification.

Preparation of Self-Supported ZnS Nanoarchitecture. ZnS nanoarchitectures were synthesized following a previously reported method.[29] By virtue of a system containing 14 M NaOH, self-supported ZnS nanoarchitectures could be thermodynamically stable and mass-produced. Briefly, 12.875 mL of 16 M NaOH solution was poured into a dried Teflon-lined autoclave with a capacity of 20 mL. A 0.167 g portion of ZnO powder was added and stirred until complete dissolution occurred. Then, 2 mL of 1 M Na_2S solution was injected into the autoclave. After stirring for about 2 min, the autoclave was sealed and heated at 230 °C for at least 12 h. The autoclave was rapidly quenched to room temperature after the hydrothermal reaction. The obtained white precipitates were centrifuged, rinsed with distilled water 5 times, then acidified with dilute acetic acid to eliminate the photocarrier quenching centers (−OH groups) capping on the as-synthesized ZnS surface, and finally dried in a vacuum oven at 60 °C. For comparison, 3-nm ZnS nanoparticles were also prepared using a facile chemical precipitation method.[30]

Preparation of Au/ZnS Nanoarchitecture Hybrids. The Au/ZnS catalysts were prepared by dispersing 0.2 g of the above-synthesized ZnS nanoarchitectures in 50 mL of water containing different amount of $HAuCl_4{\cdot}4H_2O$ (8.4, 16.7, 25.1 mg). After adjusting the pH to about 7 with 1 mM NaOH, the solution was stirred at 80 °C for 3 h. The products were collected by centrifugation, washed thoroughly with water until Cl^- was below detection, and dried at 60 °C for 12 h. The obtained powders were calcined in vacuum at 200 °C for 1 h. The nominal weight ratios of Au to ZnS (R_{Au}) were 0, 2, 4, and 6 wt %, and the samples were labeled as AZ0, AZ2, AZ4, and AZ6, respectively.

Characterization. X-ray diffraction (XRD) was used to identify the crystal structures and phase compositions of the samples. Diffraction data were collected on a PANalytical X'Pert PRO diffractometer with Cu Kα radiation (40 kV × 40 mA) and an X'Celerator detector in the continuous mode. The 2θ scanning range was from 5° to 65° with a scanning speed of 4°/min. Scanning electronic microscopy (SEM, JEOL, JSM-6700F) analyses were used to determine the particle size and morphology. Further morphological and structural characterization was based on transmission electron microscopy (TEM) and high-resolution transmission microscopy (HRTEM) observation. TEM/HRTEM analyses were conducted on a JEM-2010 electron microscope at an acceleration voltage of 200 kV. X-ray photoelectron spectroscopy (XPS) was utilized to identify the chemical status of Au in the obtained Au/ZnS catalysts. XPS measurements were performed on a Thermo Scientific ESCALAB 250 system with Mg Kα source. All the binding energies were calibrated by C 1s peak at 284.8 eV of the surface adventitious carbon. The Brunauer−Emmett−Teller (BET) surface area of the powders was measured using a Micrometrics ASAP 2020 system after the sample was degassed in vacuum at 120 °C overnight. The BET surface area was determined by a multipoint BET method using adsorption data in the relative pressure (P/P_0) range of 0.05−0.25. A desorption isotherm was used to determine the pore size distribution by the Barret−Joyner−Halenda (BJH) method, assuming a cylindrical pore model. Diffuse reflectance UV−vis spectra of the samples were collected for the dry-pressed tablets using a Shimadzu UV-2550 UV−vis spectrophotometer equipped with an integrating sphere. The $BaSO_4$ plate was used as a standard. The absorption spectra can be further calculated from the reflectance spectra using the Kubelka−Munk function, $K/S = (1-R)^2/2R$, where K is the absorption coefficient, R is the diffused reflectance, and S is the scattering coefficient.

Photocatalytic H_2 Production Activity. The photocatalytic hydrogen production experiments were performed in a 100-mL 3-neck Pyrex flask at ambient temperature and atmospheric pressure, and outlets of the flask were sealed with silicone rubber septum. A 350 W xenon arc lamp, which was positioned 20 cm away from the reactor, was used as a light source to trigger the photocatalytic reaction. The focused intensity on the flask was about 20 mW/cm^2. In a typical photocatalytic experiment, 50 mg of catalyst was dispersed by a constant stirring in 80 mL of mixed aqueous solution containing 0.35 M Na_2S and 0.25 M Na_2SO_3. Before irradiation, the system was bubbled with nitrogen for 40 min to remove the dissolved oxygen and ensured that the reaction system was under an anaerobic condition. A 0.4 mL portion of gas was sampled through the septum, and hydrogen was analyzed by gas chromatograph (GC-14C, Shimadzu, Japan, TCD, nitrogen as a carrier gas and 5 Å molecular sieve column). All glassware was carefully rinsed with distilled water prior to use. The apparent quantum efficiency (QE) was measured under the same photocatalytic reaction condition. Four low-power 365-nm LEDs (3 W) (Shenzhen LAMPLIC Science Co. Ltd. China), which were positioned 1 cm away from the reactor in four different directions, were used as light sources to trigger the photocatalytic reaction. The focused intensity for each 365-nm LED was about 80 mW/cm^2. The QE was calculated according to eq 1:

$$\mathrm{QE}[\%] = \frac{\text{number of reacted electrons}}{\text{number of incident photons}} \times 100 = \frac{\text{number of evolved } H_2 \text{molecules} \times 2}{\text{number of incident photons}} \times 100 \quad (1)$$

RESULTS AND DISCUSSION

Phase Structure and Morphology. The crystal structure and phase composition of the samples were investigated using XRD. Figure 1 shows the XRD patterns of the samples with different Au contents. XRD data reveals that the main phase of all the samples can be identified as the self-supported ZnS nanoarchitectures with interwoven wurtzite (001) nanosheets, which is consistent with our previous work.[31] In detail, the strong and sharp peak at 27.2° can be indexed as the (100) reflection of wurtzite ZnS. The adjacent broadened peak is the overlapping peaks of wurtzite (002), sphalerite (111), and wurtzite (101). For samples with higher R_{Au} ratios (AZ4 and AZ6), very weak peaks belonging to Au(111) diffraction are observed at 2$\theta \sim 38°$, indicating the presence of metallic Au.

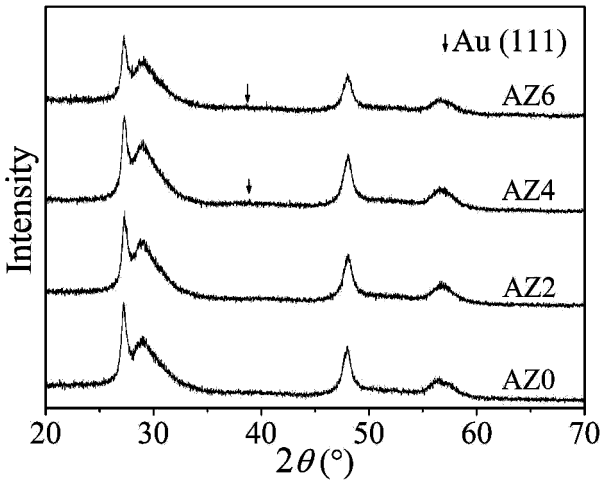

Figure 1. XRD patterns of the Au/ZnS nanoarchitecture samples with R_{Au} (wt%) = 0 (AZ0), 2 (AZ2), 4 (AZ4), 6(AZ6), respectively.

The detailed characterization of morphologies and crystal structures of the samples was performed using SEM and TEM/HRTEM. Figure 2a and 2b show typical SEM images of ZnS

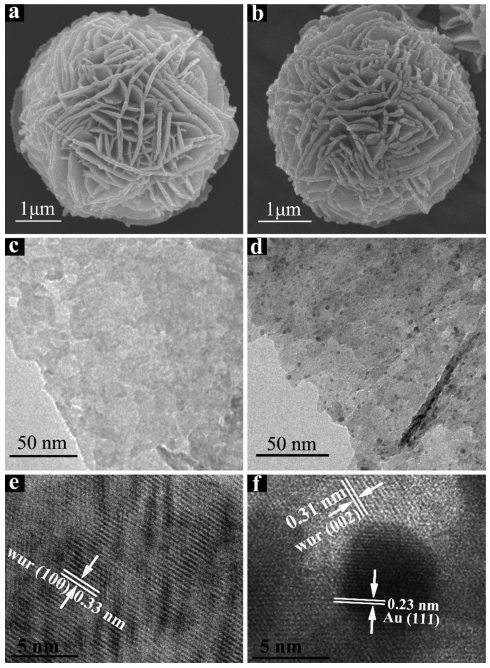

Figure 2. SEM (a and b), TEM (c and d), and HRTEM (e and f) images for Au/ZnS nanoarchitecture samples with R_{Au} (wt %) = 0 (AZ0) and 6 (AZ6), respectively.

nanoarchitectures without and with Au deposition (AZ0 and AZ6), respectively. The SEM images clearly demonstrate that ZnS microspheres composed of interwoven nanosheets were successfully fabricated by the hydrothermal method, and their morphologies remain essentially unchanged after subsequent heat treatment and Au nanoparticle deposition.

Figure 2c and 2d show a comparison of TEM images of the sample AZ0 and AZ6. It can be seen that after Au deposition, uniform black dots with an average size of 5 nm were homogeneously dispersed on the ZnS support. Further HRTEM observation indicates that the distances between the adjacent lattice fringes for AZ0 (Figure 2e) are about 0.33 nm, in agreement with the (100) d spacing for wurtzite ZnS (JCPDS No. 79-2204). As for the sample of AZ6, besides the lattice fringes with d spacing of 0.31 nm corresponding to the (002) plane of wurtzite ZnS, another kind of lattice fringes with d spacing of 0.23 nm for the black dots can be found in the HRTEM image (Figure 2f), which can be indexed as the (111) plane of face-centered cubic Au (JCPDS No. 04-0784). Therefore, the black dots can be identified as Au nanoparticles.

Chemical States of Au. XPS was further employed to identify the chemical states of Au element. Figure 3 gives a

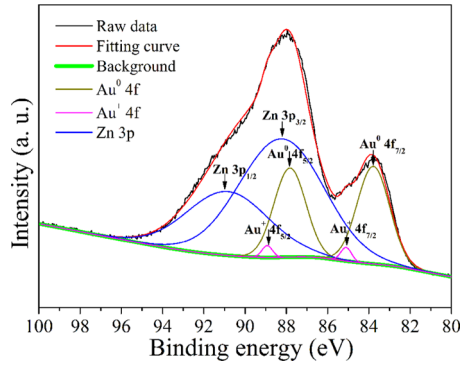

Figure 3. High-resolution XPS spectrum of Au 4f and Zn3p for the AZ6 sample.

typical high-resolution XPS spectrum of Au 4f for AZ6, in which part of the Au $4f_{5/2}$ peak is overlapped by the signal of Zn 3p. The XPS data were analyzed by fitting to a Gaussian–Lorentzian function and using a Shirley background subtraction.[32] As shown in Figure 3, the spectrum can be decomposed into six components, which can be assigned to the peaks of Au^0 $4f_{7/2}$, Au^0 $4f_{5/2}$, Au^+ $4f_{7/2}$, Au^+ $4f_{5/2}$, Zn $3p_{3/2}$, and Zn $3p_{1/2}$. It can be derived from the XPS results that the Au constituent in AZ6 is mainly in the metallic state. In addition to the metallic Au, a small amount of monovalent ions (Au(I)) also exist in the Au-loaded samples and may be incorporated into the ZnS nanoarchitectures during the heat treatment process (see discussion below).

UV–vis Absorption Properties. Figure 4 shows the UV–vis diffuse absorption spectra for samples AZ0, AZ2, AZ4 and AZ6. As can be seen, the absorbances of our samples in the UV-light region initially increase with the increasing of Au loading amount but then decrease for the sample AZ6. As for our system, UV light is mostly absorbed by ZnS. The presence of a

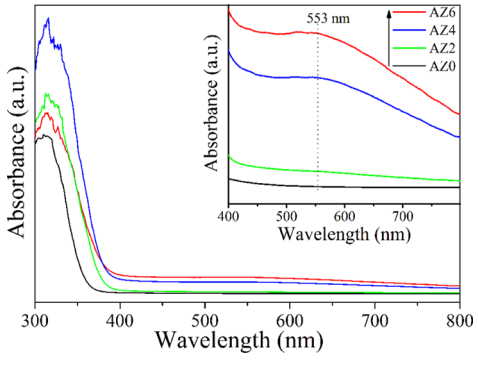

Figure 4. Comparison of UV–vis absorbance spectra of pristine (AZ0) and Au-decorated ZnS nanoarchitecture (AZ2, AZ4, and AZ6).

Table 1. Effects of R_{Au} on the Physical Properties and Photocatalytic Activities of the Samples

samples	R_{Au} (%)	S_{BET} (m^2/g)	pore volume (cm^3/g)	average pore size (nm)	band gap (eV)	activity (μmol h^{-1} g^{-1})	QE (%)
AZ0	0	128	0.39	9.6	3.59	1602	4.8
AZ2	2	116	0.40	10.1	3.48	2288	5.6
AZ4	4	109	0.40	10.5	3.43	3306	7.5
AZ6	6	108	0.38	10.1	3.41	1532	4.7
Nano	0	150	0.15	3.7		276	0.7

small amount of Au nanoparticles can accelerate the separation of the photogenerated charge carriers and thus improve the light-absorption efficiency of ZnS. However, as the surface of ZnS is covered by more Au nanoparticles, the incident UV light is gradually blocked, which leads to the decrease in the absorbance. On the other hand, with increasing Au content, all Au-loaded samples obviously exhibit an increasing absorption in the visible-light range, which is probably due to the SPR effect of metallic Au deposited on the ZnS surface. The absorption peak at about 553 nm can be assigned to the characteristic SPR peak of Au nanoparticles.[28] Therefore, Au loading can indeed extend the light response of ZnS nanoarchitecture to visible-light region. It can also be found that, as the Au content increases, the optical absorption edges of the samples shift to longer wavelengths. We determined the band gaps of the samples by fitting the optical transition at the absorption edges using the Tauc/David-Mott model[33] described by equation $(h\nu\alpha)^{1/n} = A(h\nu - E_g)$, where h is Planck's constant, ν is frequency of vibration, α is the absorption coefficient, E_g is the band gap, and A is a proportionality constant. The value of the exponent n denotes the nature of the sample transition and $n = 0.5$ when assuming a direct allowed transition. As listed in Table 1, band gaps of the samples tend to become narrower with increasing Au content. The phenomenon of band gap narrowing may be caused by Au(I) incorporation. It was reported that Au_2S is a narrow-band gap semiconductor with E_g in the range from 1.3 to 2.6 eV.[34] Therefore, alloying with Au_2S can effectively narrow the band gap of ZnS and extend its light absorption range. According to the XPS results, a small portion of Au additive exists in the form of Au(I). During the heat treatment process, Au(I) ions can be incorporated into the lattice of ZnS, which may be responsible for the band gap narrowing.

BET Surface Areas and Pore Size Distributions. Figure 5 shows the nitrogen adsorption−desorption isotherms at 77 K together with the pore size distributions (the inset) for the AZ0 and AZ6 samples. Nitrogen adsorption−desorption measurements on these two samples result in type IV isotherms with hysteresis loops according to the IUPAC classification,[35] indicating the presence of mesopores. In addition, the adsorption branches of the isotherms increase rapidly at relative pressures close to unity, which bear some resemblance to type II isotherms. Therefore, there are also macropores in the samples. The hysteresis loops can be categorized as type H3 associated with slit-like mesopores, which is consistent with the characteristic of our ZnS hierarchical nanoarchitectures. The pore size distribution curves (the inset in Figure 5) indicate that both AZ0 and AZ6 possess mesopores and macropores in a wide size range of 2 to over 60 nm. It should be noted that the sharp peaks at about 3.6 nm in the pore-size distribution curves are artifacts of the BJH method arising from the tensile strength effect (TSE). The TSE artifact appears when the desorption isotherm used for BJH analysis exhibit a sudden drop at $p/p_0 \sim 0.45$.[36,37] The other Au/ZnS nanoarchitecture samples exhibit similar nitrogen adsorption−desorption behaviors. The BET specific surface areas, pore volumes, and average pore sizes of all the samples are summarized in Table 1. As listed in Table 1, the pristine ZnS nanoarchitectures (AZ0) have a relatively high BET specific surface area (S_{BET}) up to 128 m^2/g. After Au nanoparticle deposition, the S_{BET} of the samples slightly decrease with the increasing Au content, while the pore volumes as well as the average pore sizes do not change appreciably. The decrease of the S_{BET} is because the specific surface area (m^2/g) is expressed per gram of the samples, which contain some amount of heavy Au. The densities of Au and ZnS are 19.3 and 3.98 g/cm^3, respectively. Consequently, the densities of the Au/ZnS samples increase with increasing Au amount, resulting in the reduction of the BET surface area.[10a]

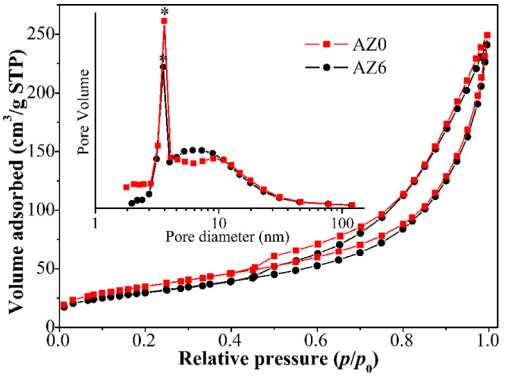

Figure 5. Nitrogen adsorption−desorption isotherms and the corresponding pore size distributions (the inset) calculated by the BJH method for AZ0 and AZ6. Asterisks (*) denote the artifacts of the BJH model.

Photocatalytic Activity. Photocatalytic H_2 production activities of Au/ZnS nanoarchitectures were evaluated under 350W xenon arc lamp using mixed 0.35 M Na_2S and 0.25 M Na_2SO_3 aqueous solutions as scavenger. The results are shown in Figure 6 and Table 1. H_2 production rate of 3-nm ZnS nanoparticles under the same experimental conditions was also evaluated for comparison. As can be seen in Figure 6 and Table 1, the pristine ZnS nanoarchitectures exhibit relatively high H_2 production activity up to 1602 μmol h^{-1} g^{-1} even without noble-metal loading, which is much higher than that of the 3-nm nanoparticles, though the nanoparticles possess a larger S_{BET}. In our previous work, we found that annealing at 200 °C for a short time can significantly improve the lattice integrity and crystallinity of the ZnS nanoarchitectures and thus optimize their photocatalytic H_2 production activities.[14] Therefore, the high H_2 production activities of the ZnS nanoarchitectures in this work may be partly credited to the high lattice integrity achieved during the calcine step in the Au loading process. On the contrary, for the 3-nm nanoparticles synthesized by our method, their photocatalytic activities were seriously constrained by the fast charge recombination resulting

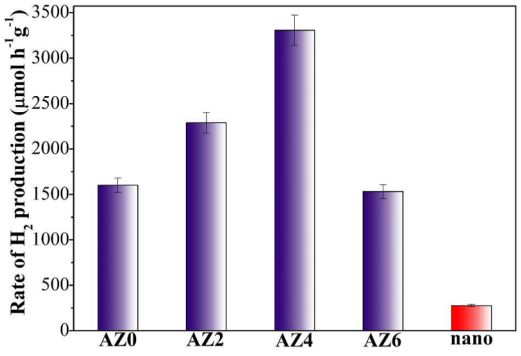

Figure 6. Comparison of photocatalytic H_2 production activities of Au/ZnS nanoarchitectures (AZ0 ~ AZ6) and 3-nm ZnS nanoparticles (nano) from mixed 0.35 M Na_2S and 0.25 M Na_2SO_3 aqueous solutions.

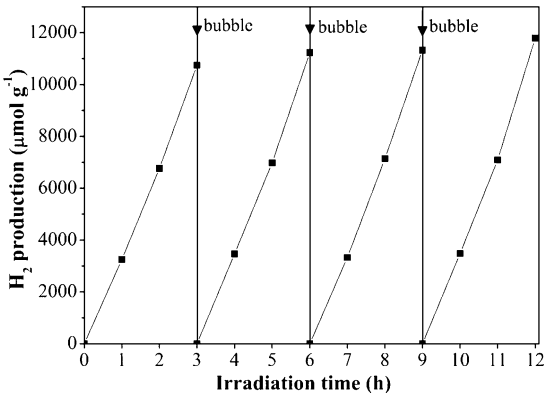

Figure 7. Time course of photocatalytic H_2 production for sample AZ4. The reaction system was bubbled with N_2 for 30 min every 3 h to remove the H_2 inside.

from the lattice distortion and lattice defects.[30b] In addition, our flower-like ZnS nanoarchitestures are composed of 20−30 nm interwoven nanosheets with wurtzite ZnS (0001) face as the exposing crystal face. Owing to the atomic arrangement of the [0001] direction of ZnS, a spontaneous polarization is induced across the wurtzite ZnS (0001) face from Zn-terminated plane to S-terminated plane.[14] There exists an internal electric field in the nanosheets induced by the spontaneous polarization, which will facilitate the separation of the photogenerated electrons and holes, and accelerate their migration to the surface. Therefore, compared with common nanoparticles, ZnS materials with dominant {0001} facets may exhibit relatively high photocatalytic activities.

It also can be seen that the presence of a small amount of Au nanoparticles can substantially improve the activity of ZnS nanoarchitectures. The photocatalytic H_2 production rates of the samples increase with increasing Au content when R_{Au} < 4%, and reach a remarkable maximum value of 3306 μmol h^{-1} g^{-1} with apparent quantum efficiency (QE) up to 7.5% at 365 nm (for AZ4). However, further increasing of R_{Au} to 6% leads to a reduction of the photocatalytic activity, which is comparable with that of the pristine ZnS nanoarchitectures. This reduction is probably due to the increase of opacity and light scattering of samples with higher Au contents, which actually reduced the effective irradiation absorbed by the reaction suspension solution.[10] Furthermore, excessive noble metal clusters may in turn work as recombination centers and thus hinder the photocatalytic hydrogen production reaction.[38,39] To evaluate the stability of our photocatalysts, a recycling test was performed on the hydrogen production activity of the sample AZ4 (Figure 7). After four recycles, the catalyst does not exhibit any loss of activity, indicating its good stability during the photocatalytic reaction. In addition, it can be found that after the first cycle, the average rate of hydrogen production is slightly increased because the hydrogen production reaction is an activated process, and the photons absorbed on the surface of the photocatalyst increase with increasing irradiation time.[17a]

It is generally accepted that noble metal loading can significantly improve the efficiency of a semiconductor photocatalyst.[10] As for our ZnS nanoarchitectures, the photocatalytic hydrogen production rate was improved by over 2 times via 4% (wt) Au-nanoparticle decoration. Considering the comparable S_{BET} of the samples, this improvement could be ascribed to the following two reasons. First, considering the lower Fermi level of Au with respect to the conduction band minimum (CBM) of ZnS, the photogenerated electrons in ZnS can readily be transferred to Au nanoparticles, which could efficiently separate the photogenerated carriers and finally result in enhancement of photocatalytic activity (see Figure 8a). Second, in our

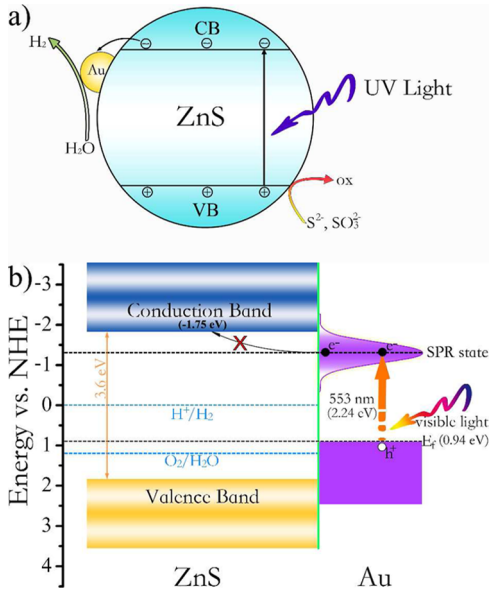

Figure 8. Schematic illustration of (a) the enhancing mechanism on photocatalytic activities of Au-loaded ZnS under UV irradiation and (b) the configuration between the Au SPR state and ZnS energy band.

experimental conditions, a small amount of Au(I) was incorporated into the ZnS lattice and narrowed the band gap of ZnS. Therefore, the light absorption region was extended, and the utilization efficiency of light irradiation was improved.

It is reported that the SPR effect of a noble metal can endow the wide-band gap semiconductors, such as TiO_2 and ZnO, with visible-light photocatalytic activities.[40] A classical mechanism is analogous to dye sensitization.[27] When plasmonic-metal nanostructures absorb visible light, the electrons near the Fermi level are excited to the SPR state (generally above the CBM of the semiconductors), injected into the conduction band of the semiconductors, and then participate in the photocatalytic reactions. Therefore, under appropriate visible light irradiation,

dx.doi.org/10.1021/am302726y | ACS Appl. Mater. Interfaces 2013, 5, 1031−1037

the photocatalytic activities of a noble metal/semiconductor system could be greatly boosted. However, unexpectedly, though our Au/ZnS nanoarchitectures do exhibit SPR absorption properties, all of them are inactive for photocatalytic hydrogen production in the visible-light region (λ > 420 nm). To find a reasonable explanation, the relative position of the SPR state of noble metal and the semiconductor energy band, as well as the electron transfer processes upon visible-light excitation should be taken into account. Figure 8b depicts a sketch of the configuration of Au SPR state and ZnS energy band. As can be seen, the Fermi level of Au lies at −5.38 eV vs vacuum (0.94 V vs NHE).[41] Under the irradiation of 553-nm visible light ($h\nu \sim 2.24$ eV), the SPR of Au nanoparticles will be induced. Thus, the energy position of the SPR state for our Au nanoparticles is about −1.3 eV vs NHE. However, to our knowledge, the conduction band minimum of ZnS lies more negative than −1.75 eV on NHE scale (higher than the SPR state of Au nanoparticles).[42−45] Therefore, in the Au/ZnS system, the excited energetic electrons in the SPR state cannot be injected in the conduction band of ZnS and thus cannot participate in the hydrogen-evolution reaction on the surface of ZnS.

CONCLUSIONS

In summary, we have successfully decorated the ZnS nanoarchitectures with highly dispersed and uniform Au nanoparticles by a simple deposition-precipitation method. The photocatalytic hydrogen production rates of these nanoarchitectures are significantly enhanced in the presence of the Au cocatalysts and reach the highest value at R_{Au} = 4% wt. At the optimal Au loading concentration, the hydrogen production rate is up to 3306 μmol h^{-1} g^{-1} with apparent quantum efficiency (QE) of 7.5% at 365 nm. On the basis of the above discussion, Au cocatalysts may play two roles in the improvement of the hydrogen production rate. First, Au loading can greatly accelerate the separation of the photogenerated charge carriers. Second, the band gap of ZnS is narrowed by the incorporation of a small portion of Au(I) and thus the utilization efficiency of light irradiation is enhanced. It is worth noting that although strong SPR absorption of the Au nanoparticles was found in our Au loading samples at the wavelength of 553 nm, all of these samples exhibit no activities in the visible light region (λ > 420 nm). According to our discussion, this should be ascribed to the highly negative reduction potential of the ZnS conduction band minimum, which prevents the excited energetic electrons in the SPR state from injecting into the conduction band. Therefore, in utilizing the SPR effect to achieve visible-light activities in the plasmonic-metal nanostructure/wide-band gap semiconductor systems, the configuration of the Fermi level of the metal, the SPR state, and the conduction band minimum of the semiconductor should be given full consideration. Generally, semiconductors with lower conduction band, such as TiO_2, ZnO and CdS, are more appropriate for plasmonic-metal nanostructure sensitization.

AUTHOR INFORMATION

Corresponding Author

*E-mail: fhuang@fjirsm.ac.cn (F.H.), jiaguoyu@yahoo.com (J.Y.).

Author Contributions

The manuscript was written through contributions of all authors. All authors have given approval to the final version of the manuscript.

Notes

The authors declare no competing financial interest.

ACKNOWLEDGMENTS

This work was supported by the National Basic Research Program of China (973 Program, 2010CB933501, 2013CB934302), the National Natural Science Foundation of China (20971123, 21273237, 51102232, and 21007070), the Fujian National Natural Science Foundation of China (2010J01054, 2010J06006), the NNSF Outstanding Youth Fund (21125730, 50625205), and the Knowledge Innovation Program of the Chinese Academy of Sciences (KJCX2-YW-N50, KJCX2-EW-J02).

REFERENCES

(1) Cortright, R. D.; Davda, R. R.; Dumesic, J. A. *Nature* **2002**, *418*, 964−967.
(2) Tollefson, J. *Nature* **2010**, *464*, 1262−1264.
(3) Hansel, A.; Lindblad, P. *Appl. Microbiol. Biotechnol.* **1998**, *50*, 153−160.
(4) Turner, J. A. *Science* **2004**, *305*, 972−974.
(5) Fujishima, A.; Honda, K. *Nature* **1972**, *238*, 37−38.
(6) Yang, X. Y.; Wolcott, A.; Wang, G. M.; Sobo, A.; Fitzmorris, R. C.; Qian, F.; Zhang, J. Z.; Li, Y. *Nano Lett.* **2009**, *9*, 2331−2336.
(7) Feng, X. J.; LaTempa, T. J.; Basham, J. I.; Mor, G. K.; Varghese, O. K.; Grimes, C. A. *Nano Lett.* **2010**, *10*, 948−952.
(8) Zhang, J. S.; Chen, X. F.; Takanabe, K.; Maeda, K.; Domen, K.; Epping, J. D.; Fu, X. Z.; Antonietti, M.; Wang, X. C. *Angew. Chem., Int. Ed.* **2010**, *49*, 441−444.
(9) He, C. Y.; Wu, X. L.; Shen, J. C.; Chu, P. K. *Nano Lett.* **2012**, *12*, 1545−1548.
(10) (a) Yu, J. G.; Qi, L. F.; Jaroniec, M. *J. Phys. Chem. C* **2010**, *114*, 13118−13125. (b) Xiang, Q. J.; Yu, J. G.; Jaroniec, M. *J. Am. Chem. Soc.* **2012**, *134*, 6575−6578. (c) Li, Q.; Guo, B. D.; Yu, J. G.; Ran, J. R.; Zhang, B. H.; Yan, H. J.; Gong, J. R. *J. Am. Chem. Soc.* **2011**, *133*, 10878−10884.
(11) Reber, J. F.; Meier, K. *J. Phys. Chem.* **1984**, *88*, 5903−5913.
(12) Hu, J. S.; Ren, L. L.; Guo, Y. G.; Liang, H. P.; Cao, A. M.; Wan, L. J.; Bai, C. L. *Angew. Chem., Int. Ed.* **2005**, *44*, 1269−1273.
(13) Zhang, J.; Yu, J. G.; Zhang, Y. M.; Li, Q.; Gong, J. R. *Nano Lett.* **2011**, *11*, 4774−4779.
(14) Hong, Y. P.; Zhang, J.; Wang, X.; Wang, Y. J.; Lin, Z.; Yu, J. G.; Huang, F. *Nanoscale* **2012**, *4*, 2859−2862.
(15) Xiong, S. L.; Xi, B. J.; Wang, C. M.; Xu, D. C.; Feng, X. M.; Zhu, Z. C.; Qian, Y. T. *Adv. Funct. Mater.* **2007**, *17*, 2728−2738.
(16) Li, Z. P.; Liu, B. B.; Yu, S. D.; Wang, J. H.; Li, Q. J.; Zou, B.; Cui, T. A.; Liu, Z. X.; Chen, Z. G.; Liu, J. *J. Phys. Chem. C* **2011**, *115*, 357−361.
(17) (a) Zhang, J.; Liu, S. W.; Yu, J. G.; Jaroniec, M. *J. Mater. Chem.* **2011**, *21*, 14655−14662. (b) Zhang, J.; Yu, J. G.; Jaroniec, M.; Gong, J. R. *Nano Lett.* **2012**, *12*, 4584−4589. (c) Yu, J. G.; Zhang, J.; Jaroniec, M. *Green Chem.* **2010**, *12*, 1611−1614.
(18) Li, Y. X.; Chen, G.; Zhou, C.; Sun, J. X. *Chem. Commun.* **2009**, 2020−2022.
(19) Zhang, W.; Zhong, Z. Y.; Wang, Y. S.; Xu, R. *J. Phys. Chem. C* **2008**, *112*, 17635−17642.
(20) Ding, S. J.; Yin, X.; Lu, X. J.; Wang, Y. M.; Huang, F. Q.; Wan, D. Y. *ACS Appl. Mater. Interfaces* **2012**, *4*, 306−311.
(21) Franco, A.; Neves, M. C.; Carrott, M. M. L. R.; Mendonca, M. H.; Pereira, M. I.; Monteiro, O. C. *J. Hazard. Mater* **2009**, *161*, 545−550.
(22) Sun, Z. H.; Yang, Z.; Zhou, J. H.; Yeung, M. H.; Ni, W. H.; Wu, H. K.; Wang, J. F. *Angew. Chem., Int. Ed.* **2009**, *48*, 2881−2885.

(23) De, G. C.; Roy, A. M.; Bhattacharya, S. S. *Int. J. Hydrogen Energy* **1996**, *21*, 19−23.
(24) Chen, W. T.; Hsu, Y. J. *Langmuir* **2010**, *26*, 5918−5925.
(25) Zhang, X. J.; Jin, Z. L.; Li, Y. X.; Li, S. B.; Lu, G. X. *Appl. Surf. Sci.* **2008**, *254*, 4452−4456.
(26) Kandiel, T. A.; Ismail, A. A.; Bahnemann, D. W. *Phys. Chem. Chem. Phys.* **2011**, *13*, 20155−20161.
(27) (a) Linic, S.; Christopher, P.; Ingram, D. B. *Nat. Mater.* **2011**, *10*, 911−921. (b) Zhou, X. M.; Liu, G.; Yu, J. G.; Fan, W. H. *J. Mater. Chem.* **2012**, *22*, 21337−21354.
(28) Zhu, S. Y.; Liang, S. J.; Gu, Q.; Xie, L. Y.; Wang, J. X.; Ding, Z. X.; Liu, P. *Appl. Catal., B* **2012**, *119*, 146−155.
(29) Li, D. S.; Lin, Z.; Ren, G. Q.; Zhang, J.; Zheng, J. S.; Huang, F. *Cryst. Growth Des.* **2008**, *8*, 2324−2328.
(30) (a) Zhang, J.; Lin, Z.; Lan, Y. Z.; Ren, G. Q.; Chen, D. G.; Huang, F.; Hong, M. C. *J. Am. Chem. Soc.* **2006**, *128*, 12981−12987. (b) Ren, G. Q.; Lin, Z.; Wang, C.; Liu, W. Z.; Zhang, J.; Huang, F.; Liang, J. K. *Nanotechnology* **2007**, *18*, 035705.
(31) Hong, Y. P.; Lin, Z.; Huang, J.; Wang, Y. J.; Huang, F. *Nanoscale* **2011**, *3*, 1512−1515.
(32) Shirley, D. A. *Phys. Rev. B* **1972**, *5*, 4709−4714.
(33) Li, X. M.; Zhu, H. W.; Wei, J. Q.; Wang, K. L.; Xu, E. Y.; Li, Z.; Wu, D. H. *Appl. Phys. A: Mater. Sci. Process.* **2009**, *97*, 341−344.
(34) Mikhlin, Y.; Likhatski, M.; Karacharov, A.; Zaikovski, V.; Krylov, A. *Phys. Chem. Chem. Phys.* **2009**, *11*, 5445−5454.
(35) Sing, K. S. W.; Everett, D. H.; Haul, R. A. W.; Moscou, L.; Pierotti, R. A.; Rouquerol, J.; Siemieniewska, T. *Pure Appl. Chem.* **1985**, *57*, 603−619.
(36) Kanyo, T.; Konya, Z.; Kukovecz, A.; Berger, F.; Dekany, I.; Kiricsi, I. *Langmuir* **2004**, *20*, 1656−1661.
(37) Janssen, A. H.; Koster, A. J.; de Jong, K. P. *J. Phys. Chem. B* **2002**, *106*, 11905−11909.
(38) Sun, F. Z.; Qiao, X. L.; Tan, F. T.; Wang, W.; Qiu, X. L. *J. Mater. Sci.* **2012**, *47*, 7262−7268.
(39) Sreethawong, T.; Yoshikawa, S. *Catal. Commun.* **2005**, *6*, 661−668.
(40) Wang, P.; Huang, B. B.; Dai, Y.; Whangbo, M. H. *Phys. Chem. Chem. Phys.* **2012**, *14*, 9813−9825.
(41) Uda, M.; Nakamura, A.; Yamamoto, T.; Fujimoto, Y. *J. Electron. Spectrosc.* **1998**, *88*, 643−648.
(42) Roy, A. M.; De, G. C. *J. Photochem. Photobiol. A* **2003**, *157*, 87−92.
(43) Reber, J. F.; Rusek, M. *J. Phys. Chem.* **1986**, *90*, 824−834.
(44) Li, D. S.; Huang, F.; Ren, G. Q.; Zhuang, Z. Y.; Pan, D. M.; Lin, Z. *J. Nanosci. Nanotechnol.* **2009**, *9*, 6721−6725.
(45) Yu, X. X.; Yu, J. G.; Cheng, B.; Huang, B. B. *Chem.—Eur. J.* **2009**, *15*, 6731−6739.